

Empirical Constraints of Super-Galactic Winds at $z \gtrsim 0.5$

Jean-René Gauthier^{1*} and Hsiao-Wen Chen^{2†}

¹*Cahill Center for Astronomy and Astrophysics, California Institute of Technology, Pasadena CA 91125 USA*

²*Department of Astronomy & Astrophysics and Kavli Institute for Cosmological Physics, University of Chicago, Chicago IL 60637 USA*

24 October 2021

ABSTRACT

Under the hypothesis that Mg II absorbers found near the minor axis of a disk galaxy originate in the cool phase of super-galactic winds, we carry out a study to constrain the properties of large-scale galactic outflows at redshift $z_{\text{gal}} \gtrsim 0.5$ based on the observed relative motions of individual absorbing clouds with respect to the positions and orientations of the absorbing galaxies. We identify in the literature four highly inclined disk galaxies located within 50 kpc and with the minor axis oriented within 45 degrees of a background QSO sightline. Deep HST images of the galaxies are available for accurate characterizations of the optical morphologies of the galaxies. High-quality echelle spectra of the QSO members are also available in public archives for resolving the velocity field of individual absorption clumps. Three galaxies in our sample are located at $\rho = 8 - 34$ kpc and exhibit strong associated Mg II absorption feature with $W_r(2796) \gtrsim 0.8 \text{ \AA}$. One galaxy, located at an impact parameters $\rho = 48$ kpc, does not show an associated Mg II absorber to a $3\text{-}\sigma$ limit of $W_r(2796) = 0.01 \text{ \AA}$. Combining known morphological parameters of the galaxies such as the inclination and orientation angles of the star-forming disks, and resolved absorption profiles of the associated absorbers at $\rho < 35$ kpc away, we explore the allowed parameter space for the opening angle θ_0 and the velocity field of large-scale galactic outflows as a function of z -height, $v(z)$. We find that the observed absorption profiles of the Mg II doublets and their associated Fe II series are compatible with the absorbing gas being either accelerated or decelerated, depending on θ_0 , though accelerated outflows are a valid characterization only for a narrow range of θ_0 . Under an acceleration scenario, we compare the derived $v(z)$ with predictions from Murray et al. (2011) and find that if the gas is being accelerated by the radiation and ram pressure forces from super star clusters, then the efficiency of thermal energy input from a supernova explosion is $\epsilon \lesssim 0.01$. In addition, we adopt a power-law function from Steidel et al. (2010) for characterizing the accelerated outflows as a function of z -height, $a(z) \propto z^{-\alpha}$. We find a steep slope of $\alpha \approx 3$ for a launch radius of $z_{\text{min}} = 1$ kpc. A shallower slope of $\alpha \approx 1.5$ would increase z_{min} to beyond 4 kpc. We discuss the implications of these parameter constraints.

Key words: quasars: absorption lines – galaxies:starburst – galaxies: haloes – ISM: jets and outflows

1 INTRODUCTION

Super-galactic winds are considered a promising mechanism to eject metals into the circumgalactic and intergalactic media (e.g., Aguirre et al. 2001; Cen et al. 2005; Oppenheimer & Davé 2006; Pieri et al. 2007; Davé et al. 2010). Galactic-scale outflows are observed through a variety of techniques

and diagnostics, including detections of blueshifted self-absorption in Na I $\lambda\lambda$ 5890,5896 (e.g., Heckman et al. 2000; Rupke & Veilleux 2005; Rupke et al. 2005a) or in Mg II $\lambda\lambda$ 2796, 2803 doublet transitions (e.g., Tremonti et al. 2007; Weiner et al. 2009; Martin & Bouché 2009; Rubin et al. 2010), and resolved morphologies of hot plasma associated with supernova driven winds (e.g., Veilleux et al. 2005). While the observed outflow speed extends up to 600 – 1000 km s^{-1} (e.g., Rupke & Veilleux 2005; Rupke et al. 2005a; Weiner et al. 2009), starburst driven winds have not been

* E-mail: jrg@astro.caltech.edu

† E-mail: hchen@oddjob.uchicago.edu

directly detected beyond ~ 15 kpc from nearby star-forming regions (e.g., Heckman et al. 2002; Rubin et al. 2011).

At the same time, observations of close QSO–galaxy and galaxy–galaxy pairs have revealed chemically enriched circumgalactic medium out to 100 kpc projected distances through absorption features imprinted in the spectra of background objects (e.g., Chen et al. 2001a; Adelberger et al. 2005; Chen et al. 2010a; Steidel et al. 2010). Although there is a lack of observational evidence to physically connect outflows that produce blueshifted self-absorption in star-forming galaxies with metal enriched absorbers found at 10 – 100 kpc along transverse directions, starburst driven outflows remain as the leading scenario for explaining the presence of metal enriched absorbing clouds at large projected distances (e.g., Oppenheimer et al. 2009). In particular, many groups have attempted to connect strong metal-line absorbers such as Mg II of rest-frame absorption equivalent width $W_r(2796) \gtrsim 1 \text{ \AA}$ with star-forming galaxies (e.g., Bond et al. 2001; Zibetti et al. 2007; Chelouche & Bowen 2010; Kacprzak & Churchill 2011; Nestor et al. 2011; Matejek & Simcoe 2012; but see Gauthier & Chen 2011; Chen et al. 2010b for different empirical findings). A key result of these various studies is that star-forming galaxies at redshift $z_{\text{gal}} \sim 1$ appear to show enhanced Mg II absorption¹ at projected distances $\lesssim 50$ kpc along the minor axis (e.g., Bordoloi et al. 2011), suggesting that outflows may be a dominant contributor to the observed Mg II absorbers at least within 50 kpc of star-forming regions.

Recent analytic works have examined different physical mechanisms that could drive super-galactic winds (e.g. Murray et al. 2005, 2011). In Murray et al. (2011), the authors propose that radiation pressure from massive star clusters can drive outflows at velocities greater than the galaxy circular velocity. Once the outflowing material reaches above the star-forming disk, it is exposed to both radiation from other star-forming regions and hot gas from supernova bubbles originated in the parent galaxy. According to this model, the combination of radiation pressure and ram pressure force can accelerate and drive outflows to $\sim 50 - 100$ kpc away. Such mechanisms can be particularly efficient in low-mass galaxies undergoing strong episodes of star formation activities like M82.

Under the hypothesis that Mg II absorbers originate in super-galactic winds, empirical constraints for the geometry and dynamics of outflows can be obtained based on comparisons of line-of-sight gas kinematics and spatial orientation of the star-forming disk. Specifically, in the local universe large-scale galactic outflows are commonly found to follow a bi-conical pattern along the rotation axis of the star-forming disk (e.g., Heckman et al. 2000) with a varying degree of collimation, typically $10 - 45^\circ$ (Bland-Hawthorn et al. 2007). In this paper, we test the superwind hypothesis of the origin of Mg II absorbers and derive constraints for starburst driven outflows using pairs of QSOs and highly inclined disk galaxies found at $z_{\text{gal}} = 0.2 - 0.9$. We have identified in the literature four highly inclined disk galaxies located within 50

kpc and with the minor axis oriented within 45 degrees of a background QSO sightline. Deep *Hubble Space Telescope* (HST) images of the galaxies are available in the HST data archive for accurate characterizations of the optical morphologies of the galaxies. High-quality echelle spectra of the QSO members are available in public archives for resolving the velocity field of individual absorption clumps. We construct a conical outflow model and apply the observed gas kinematics to constrain the velocity gradient along the polar axis of each galaxy. We compare the results of our analysis with different model predictions (e.g., Steidel et al. 2010; Murray et al. 2011) and identify a plausible range for various model parameters.

This paper is organized as follows. In section 2, we describe the data and observational techniques. A description of the conic outflow model for describing the wind geometry is presented in section 3. In section 4, we present the derived constraints of the outflow model for individual galaxies. We compare the results of our study with predictions of analytical models in section 5. We adopt a Λ cosmology with $\Omega_M = 0.3$ and $\Omega_\Lambda = 0.7$, and a Hubble constant $H_0 = 70 \text{ km s}^{-1} \text{ Mpc}^{-1}$ throughout the paper. All distances are in proper rather than comoving units unless otherwise stated.

2 OBSERVATIONAL DATA AND ANALYSIS

To obtain empirical constraints for starburst driven outflows, we searched the literature and identified a small sample of close (projected distances $\rho < 50$ kpc) QSO and galaxy pairs for which the disks have an inclination angle $i_0 > 60$ degrees and a position angle of the major axis $\alpha > 45$ degrees (or minor axis < 45 degrees) from the QSO sightline. These selection criteria ensure that the QSO sightline probes the regions near the polar axis.

Our search yielded four QSO and galaxy pairs. A summary of the physical properties of the galaxies are presented in Table 1, including galaxy redshift (z_{gal}), projected distance (ρ) to the QSO sightline, rest-frame absolute B -band magnitude (M_B), inclination (i_0) and position angles (α) of the star-forming disk and, when available, the rest-frame equivalent width of [O II] emission line ($W_r([\text{O II}])$). Unfortunately, no measurement of on-going star formation rate is available for any of the galaxies in the sample. We also present in Table 1 the properties of the corresponding Mg II absorber, including the mean absorption redshift ($z_{\text{Mg II}}$) and total rest-frame absorption equivalent width ($W_r(2796)$). In the absence of a Mg II absorption feature, we place a $3\text{-}\sigma$ upper limit to $W_r(2796)$.

Deep optical HST images obtained using the Wide Field and Planetary Camera 2 (WFPC2) and the F702W filter are available for all four galaxies in the HST data archive. Morphological parameters of galaxies *A* and *B* in the field around 3C336 were adopted from Chen et al. (1998, 2001b). Galaxy *C* in the field around LBQS0058+0155 is heavily blended with the background QSO light. We adopted the inclination angle estimated by Pettini et al. (2000) and determine the position angle of the inclined disk ourselves. Galaxy *D* in the field around Q0827+243 has not been studied before. We retrieved the imaging data and determined the morphological parameters by performing a two-dimensional surface brightness profile analysis ourselves.

¹ The use of Mg II absorbers is mostly practical, because at $z \gtrsim 0.4$ the doublet transitions are redshifted into the optical window where QSO and galaxy spectra are recorded and because these transitions are strong.

Table 1. Properties of Sample Galaxies and the Associated Mg II Absorbers

QSO	Galaxy	z_{gal}	ρ (kpc)	M_B	i_0 ($^\circ$)	α ($^\circ$)	$W_r([\text{O II}])$ (\AA)	Ref ^a	$z_{\text{Mg II}}^b$	$W_r(2796)^c$ (\AA)
3C336	A	0.4721	33.6	-19.0	74	96.8		1,3	0.4715	0.82 ± 0.07
	B	0.8909	23.3	-20.3	81	124.1	≈ -13.4	1,3	0.8907	1.53 ± 0.05
LBQS0058+0155	C	0.6120	7.9	-18.4	65	113	-2.6 ± 1.1	3,5	0.6126	1.67 ± 0.01
Q0827+243	D	0.199	48.4	-19.9	85	86.3		4	0.199	< 0.01

^a[1] Steidel et al. (1997); [2] Chen et al. (2001a); [3] Chen et al. (2005); [4] Steidel et al. (2002); [5] Pettini et al. (2000).

^bWe adopt a mean absorption redshift as the redshift of the absorber.

^cTotal rest-frame absorption equivalent width summed over all components.

Echelle spectra of 3C336 and Q0827+243 were obtained using the Ultraviolet and Visual Echelle Spectrograph (UVES; D’Odorico et al. (2000)) on VLT-UT2 and was retrieved from the ESO data archive. The observations of 3C336 (program ID 069.A-0371, PI: Savaglio) and Q0827+243 (program ID 068.A-0170) were carried out using a $1''$ slit, dichroic #1, and cross-disperser CD#1, yielding a spectral resolution of $\text{FWHM} \approx 7.5 \text{ km s}^{-1}$. A sequence of three exposures of 4900 s each were obtained for 3C336 and a sequence of four exposures of 3600 s duration were obtained for Q0827+243. The data were binned 2×2 during readout. The spectra were processed and calibrated using the standard UVES reduction pipeline.

Echelle spectra of LBQS0058 + 0155 were retrieved from the Keck HIRES KOA archive. The observations of LBQS0058 + 0155 (program ID C99H, PI: Steidel) were obtained using a $0.9''$ slit (Deck C1) and the UV cross-disperser that offer a spectral resolution of $\text{FWHM} \approx 6 \text{ km s}^{-1}$. A sequence of two exposures of 3600 s each were taken. The data were binned 2×2 during readout. The spectra were processed through the MAKEE reduction pipeline, a reduction code tailored to handle HIRES data². The product of MAKEE consists of individual echelle orders, corrected for the blaze function, vacuum wavelengths, and heliocentric velocities.

Individual spectra were combined to form a final stacked spectrum per QSO, excluding deviant pixels, which was then continuum normalized based on a low-order polynomial fit to regions in the QSO spectrum that are free of narrow absorption lines. These final combined spectra were used to examine the kinematic signatures of Mg II absorbers and those of associated metal-line transitions such as Fe II, and Mn II absorption at the redshift of each galaxy listed in Table 1. The high spectral resolution and high S/N QSO spectra allow us to resolve individual absorption components and determine accurate velocity centroids of these individual clumps.

3 A CONICAL OUTFLOW MODEL

Under the hypothesis that strong Mg II absorbers uncovered near the polar axis of a star-forming galaxy are produced in super-galactic winds, here we develop a simple conical outflow model to characterize the geometry and kinematics of the outflowing gas. Specifically, we assume that the observed Mg II absorbers originate in the photo-ionized, cool phase

(with temperature $T \sim 10^4 \text{ K}$) of conical outflows which follow the path of least resistance along the polar axis.

The conical outflow model is illustrated in Figure 1, which shows the relative orientations of the inclined disk and the outflows with respect to the QSO line of sight. The collimated outflow, originated at the center of the star-forming disk, is characterized by an outward expanding cone along the polar axis \vec{z} with a total angular span of $2\theta_0$, and the size of the outflowing disk s at z is $s = z \tan \theta_0$. The star-forming disk (at $z = 0$) marked by the grey circle is inclined from the line of sight \vec{z}' by i_0 degrees. The projection of the star-forming disk on the plane of the sky (the $x'-y'$ plane) is shown in light blue with the major axis oriented at a position angle α from the QSO line of sight, which is at projected distance ρ . The QSO sightline intercepts the conical outflows at a vertical disk height z from z_1 to z_2 , which is determined by the opening angle θ_0 . The projected distances $\ell_{[1,2]}$ between the outflow disks at $z_{[1,2]}$ and the QSO sightline are related to $z_{[1,2]}$ according to $s_{[1,2]} = \ell_{[1,2]} \sqrt{1 + \sin^2 \phi_{[1,2]} \tan^2 i_0} = z_{[1,2]} \tan \theta_0$, where $\phi_{[1,2]}$ are the position angles of the projected outflow disks at $z_{[1,2]}$ (see Figure 1) and are constrained by

$$\tan \phi_{[1,2]} = \frac{\rho \sin \alpha - z_{[1,2]} \sin i_0}{\rho \cos \alpha}. \quad (1)$$

Applying the law of sines, which relates ρ and ℓ following

$$\frac{\rho}{\sin(3\pi/2 - \phi)} = \frac{\ell}{\sin(\alpha - \pi/2)} \quad (2)$$

the relation between (z_1, z_2) and the opening angle θ_0 is then formulated according to the following,

$$z_{[1,2]} \tan \theta_0 = \rho \sqrt{1 + \sin^2 \phi_{[1,2]} \tan^2 i_0} \left(\frac{\cos \alpha}{\cos \phi_{[1,2]}} \right), \quad (3)$$

where i_0 and α are the inclination and orientation angles of the star-forming disk.

Equations (1) and (3) can be generalized to calculate the appropriate θ for any given point along the QSO line of sight at z -height $z_1 \leq z \leq z_2$ (the top-right panel of Figure 1). For an absorbing clump moving outward at z height, the outflow speed v is then related to the observed line-of-sight velocity v_{los} according to

$$v = v_{\text{los}} / \cos i \quad (4)$$

where

$$i = \sin^{-1} \left(\frac{\rho}{z} \cos \theta \right), \quad (5)$$

and $\theta \leq \theta_0$.

² <http://spider.ipac.caltech.edu/staff/tab/makee/>

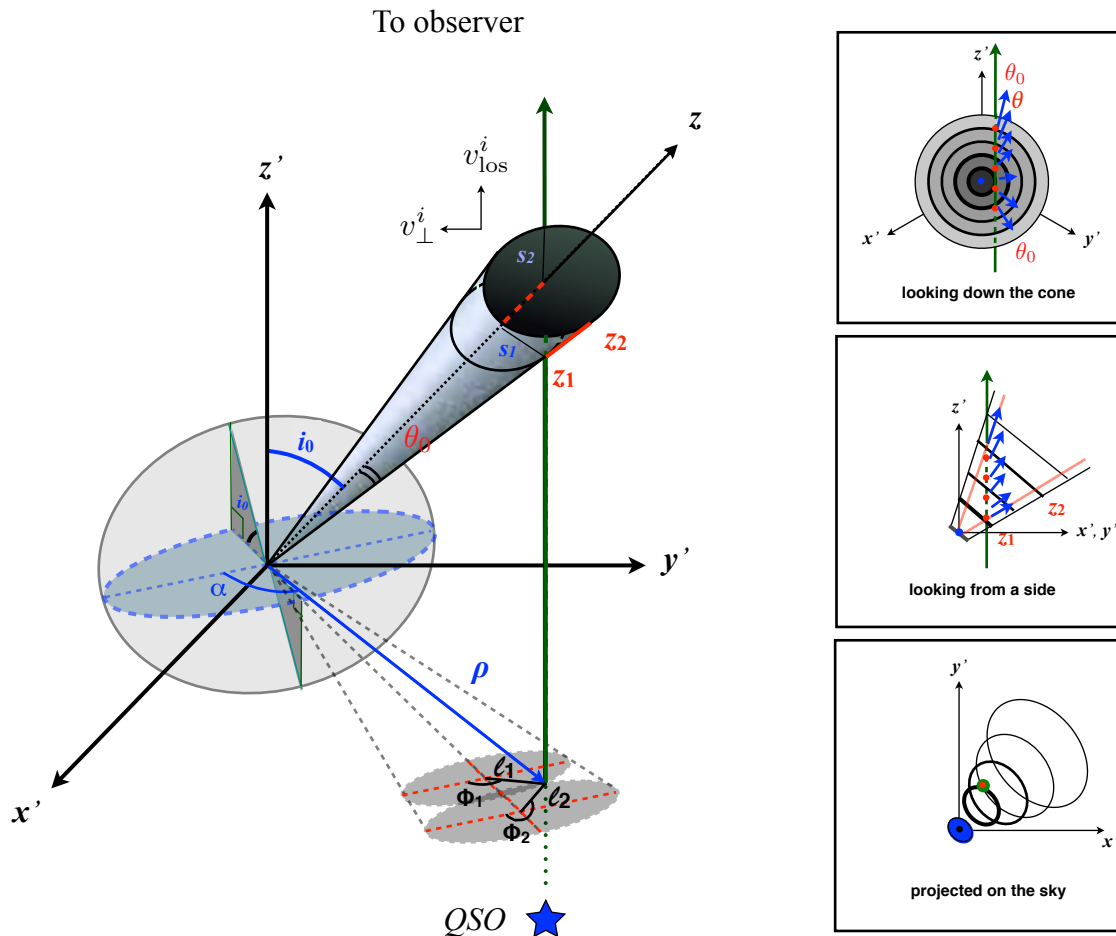


Figure 1. *Left:* Cartoon illustrating the conical outflow model in our study. In this viewing angle, the QSO line of sight runs in parallel to the \vec{z}' axis, while the x' - y' plane represents the plane of the sky. The star-forming disk is indicated by the grey circle and is inclined from the \vec{z}' axis by i_0 degrees. The projected disk on the plane of the sky is shown by the light blue ellipse oriented at a position angle of α from the QSO sightline, which is at projected distance ρ . The conical outflows follow the path of least resistance along the polar axis (\vec{z}) with a total angular span of $2\theta_0$. The solid ellipses along the conical outflows mark the disks at constant z -height in the outflows, with their projection on the plane of the sky indicated by the corresponding light grey ellipses in the x' - y' plane. The QSO line of sight enters the outflows at z_1 and exits at z_2 ($> z_1$). The size of the outflowing disk at $z_{[1,2]}$ is $s_{[1,2]} = z_{[1,2]} \tan \theta_0$. The projected distances between the outflow disks at $z_{[1,2]}$ and the QSO sightline are marked by $\ell_{[1,2]}$, which are related to $z_{[1,2]}$ according to $s_{[1,2]} = \ell_{[1,2]} \sqrt{1 + \sin^2 \phi_{[1,2]}} \tan^2 i_0 = z_{[1,2]} \tan \theta_0$. *Right:* Viewing the conical outflows in different projections. The panels show the impact geometry of the QSO sightline when looking straight down the collimated outflows (top), when looking from a side (middle), and when projected on the sky (bottom). The QSO line of sight is marked in green with the path inside the outflows highlighted in red dots. The blue arrows indicate the moving direction of the outflowing gas at an angle θ from \vec{z} .

For our study, i_0 , α , and ρ are known from HST imaging data of the galaxies, and θ_0 , which is unknown, uniquely determines the minimum and maximum z -height, z_1 and z_2 in the outflows as probed by the QSO sightline. Here we assume that the cool gas producing the observed absorption features is distributed symmetrically around the polar axis and the absorbing clumps at z_1 and z_2 probe regions close to the front and back side of the conical outflows. This is consistent with the outflow morphologies seen in local starburst galaxies (see Cooper et al. 2008 for a more detailed discussion). The goal of our study is to explore a plausible range of θ_0 and examine how the velocity of outflowing gas varies with z -height. We note that if asymmetry arises due to inhomogeneities in the outflows, then the inferred velocity

gradient (see § 5.1) represents a lower limit to the intrinsic outflow velocity field.

4 EMPIRICAL CONSTRAINTS OF INDIVIDUAL GALAXIES

Using the geometric model developed in § 3 for conical outflows, we proceed with kinematic studies of individual galaxies. For each galaxy, we take into account its known optical morphology from HST images, which determines the orientation of the conical outflows. We measure the line-of-sight velocity field of the outflows based on the resolved absorption components at the redshift of the galaxy observed in the echelle spectra of the background QSO.

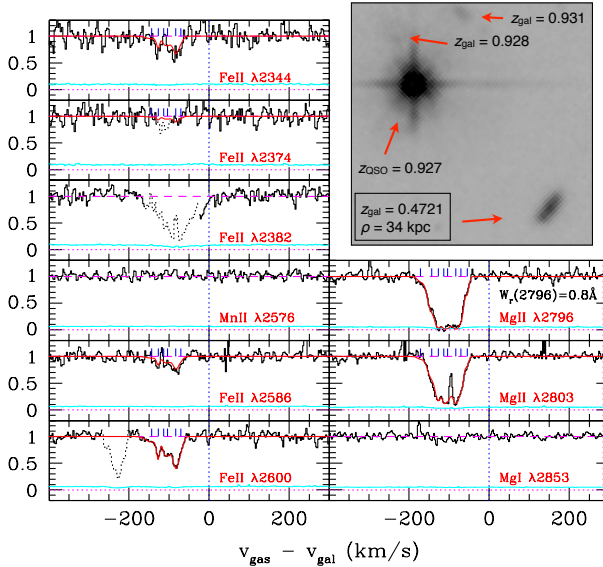


Figure 2. Line-of-sight velocity distribution of absorbing clouds at projected distance $\rho = 34$ kpc of Galaxy A at $z_{\text{gal}} = 0.472$ with $\alpha = 96.8$ degrees and $i_0 = 74$ degrees. The QSO echelle spectra cover absorption transitions due to Fe II, Mn II, Mg II, and Mg I at the redshift of the galaxy. The absorption profiles are shown in individual spectral panels. We observe strong absorption in Fe II and Mg II, but not in Mn II or Mg I transitions. In each spectral panel, the absorption spectrum is shown in solid histogram with the $1\text{-}\sigma$ error spectrum shown in thin cyan histograms. Zero velocity in each spectral panel corresponds to the systemic redshift of the galaxy at $z_{\text{gal}} = 0.4721$. Contaminating features are dotted out. A Voigt profile analysis of the observed Fe II and Mg II absorption profiles yields a minimum of eight individual absorption components and a reduced χ^2 of $\chi_r^2 = 1.1$. The best-fit model absorption profiles are shown in red curves and the positions of individual components are also marked by tickmarks at the top of individual panels. The total rest-frame Mg II absorption equivalent width over all observed components is $W_r(2796) = 0.8$ Å. The absorbing clumps display relative line-of-sight motions ranging from $\Delta v_{\text{los}} = -54.8$ km s $^{-1}$ to $\Delta v_{\text{los}} = -143.7$ km s $^{-1}$ with respect to the systemic redshift of the galaxy. The absorbing galaxy is located in the lower-right corner of the image panel. The background QSO and additional spectroscopically identified galaxies are also marked.

To measure the velocity field, we first search in the QSO echelle spectra for all absorption transitions that are associated with the galaxy. These include, in addition to the Mg II absorption doublets, the Fe II absorption series, Mn II, and Mg I absorption transitions. We then perform a Voigt profile analysis that considers all the observed absorption features at once, using the VPFIT³ software package (Carswell et al. 1991). We consider the minimum number of components required to deliver the best χ^2 in the Voigt profile analysis. Finally, we establish the observed line-of-sight velocity in the outflows by comparing the relative velocities of individual absorption component with the systemic redshift of the galaxy.

Assuming that the outflow velocity field is characterized by a smooth velocity gradient with the distance from

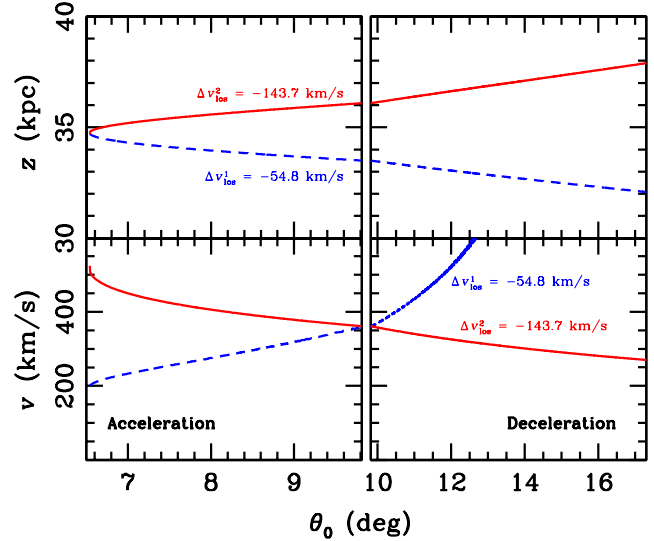


Figure 3. Allowed parameter space for the z -heights (top panels) and de-projected velocities (bottom) of individual absorbing components observed in Figure 2 versus allowed opening angle θ_0 . The minimum and maximum allowed θ_0 are constrained by the relative orientation and alignment of the star-forming disk with respect to the QSO sightline. As shown in Figure 2, the galaxy is oriented at a position angle of $\alpha = 96.8$ degrees from the QSO line of sight. In order for outflows to be responsible for the observed absorption features in the QSO spectrum, the minimum allowed opening angle is $\theta_0 \gtrsim 6.5$ degrees. In addition, all absorbing clumps are found blueshifted from the systemic redshift of the galaxy. Given that the galaxy has an inclination angle of $i_0 = 74$ degrees, the lack of redshifted absorbing components constrains the opening angle at $\theta_0 \lesssim 16$ degrees. If we further assume that the line-of-sight velocity increases smoothly from z_1 (where the QSO sightline enters the conical outflows) to z_2 (where the QSO sightline exits the conical outflows), we find that the outflows can only be accelerating if $\theta_0 \lesssim 10$ degrees. Beyond $\theta_0 \approx 10$ degrees, the absorbing clump at z_1 would have to move faster than the absorbing clump at z_2 in order to produce the observed line-of-sight velocity of $\Delta v_{\text{los}}^v = -54.8$ km s $^{-1}$, in which case the outflows would be decelerating as the gas moves further away from the star-forming disk.

the star-forming disk, we can then obtain a unique mapping between the observed velocity components and the corresponding z -heights in the conical outflow model. The observed relative motions of individual absorbing clumps along the QSO sightline, when deprojected along the polar axis according to Equations (4) and (5) for a plausible range of θ_0 , constrain the outflow velocity field as a function of z -height, $v(z)$, that can be compared directly with model predictions (e.g., Martin & Bouché 2009; Steidel et al. 2010; Murray et al. 2011). We describe the results of our analysis of individual galaxies in the following sections.

4.1 Galaxy A at $z = 0.472$ in the field around 3C 336

Galaxy A in the field around 3C 336 ($z_{\text{QSO}} = 0.927$) was spectroscopically identified at $z_{\text{gal}} = 0.4721 \pm 0.0002$ by Steidel et al. (1997). The galaxy is at projected distance $\rho = 33.6$ kpc from the QSO line of sight. Chen et al. (1998, 2001b)

³ <http://www.ast.cam.ac.uk/rfc/vpfit.html>

analyzed available HST WFPC2 images of the field (top-right panel of Figure 2) and measured $\alpha = 96.8$ degrees and $i_0 = 74$ degrees for the disk (Table 1). The echelle spectra of the QSO cover a wavelength range that allows observations of Fe II, Mn II, Mg II, and Mg I absorption at the redshift of the galaxy. The absorption profiles are shown in individual spectral panels of Figure 2. We detect strong absorption complex in Fe II and Mg II, but not in Mn II or Mg I transitions. A Voigt profile analysis that simultaneously takes into account the observed Fe II and Mg II absorption profiles yields a minimum of eight individual absorption components and $\chi_r^2 = 1.1$. The total rest-frame Mg II absorption equivalent width over all observed components is $W_r(2796) = 0.8 \pm 0.1 \text{ \AA}$. The absorbing clumps display relative line-of-sight motions ranging from $\Delta v_{\text{los}} = -54.8 \text{ km s}^{-1}$ to $\Delta v_{\text{los}} = -143.7 \text{ km s}^{-1}$ with respect to the systemic redshift of the galaxy.

Figure 2 shows that the cool gas probed by the Mg II absorption transitions is entirely blueshifted with respect to the star-forming disk with a total line-of-sight velocity spread of $\approx 90 \text{ km s}^{-1}$. Given that the galaxy is oriented at a position angle of $\alpha = 96.8$ degrees from the QSO line of sight, we note that in order for outflows to be responsible for the observed absorption features in the QSO spectrum the opening angle must exceed $\theta_0 \approx 6.5$ degrees. Furthermore, the galaxy has an inclination angle of $i_0 = 74$ degrees, and therefore the lack of redshifted absorbing components constrains the opening angle at $\theta_0 \lesssim 16$ degrees. The minimum and maximum allowed θ_0 are completely constrained by the relative orientation and alignment of the star-forming disk with respect to the QSO sightline.

For a given θ_0 , we determine the z -height at which the QSO sightline enters (z_1) and exits (z_2) the conical outflows. If we further assume that the line-of-sight velocity increases smoothly from z_1 to z_2 , we can calculate the appropriate range of de-projected velocities (v_1, v_2) probed by the QSO sightline following the framework outlined in § 3. The results are presented in Figure 3. Our calculations show that the outflows would be accelerating if $\theta_0 \lesssim 10$ degrees. Beyond $\theta_0 \approx 10$ degrees, an absorbing clump at z_1 would have to move faster than an absorbing clump at z_2 in order to produce the observed line-of-sight velocity of $\Delta v_{\text{los}}^1 = -54.8 \text{ km s}^{-1}$, in which case the outflows would be decelerating as the gas moves further away from the star-forming disk. It is straightforward to show that if we assume decreasing line-of-sight velocity from z_1 to z_2 , then the outflows can only be decelerating over the full range of allowed θ_0 .

4.2 Galaxy B at $z = 0.891$ in the field around 3C 336

Galaxy B in the field around 3C 336 ($z_{\text{QSO}} = 0.927$) was spectroscopically identified at $z_{\text{gal}} = 0.8909 \pm 0.0002$ by Steidel et al. (1997). The galaxy is at projected distance $\rho = 23.3 \text{ kpc}$ from the QSO line of sight. Chen et al. (1998, 2001b) analyzed available HST WFPC2 images of the field (top-right panel of Figure 4) and measured $\alpha = 124.1$ degrees and $i_0 = 81$ degrees for the disk (Table 1). The echelle spectra of the QSO cover a wavelength range that allows observations of Fe II, Mn II, Mg II, and Mg I absorption at the redshift of the galaxy. The absorption profiles are shown in individual spectral panels of Figure 4. We detect strong ab-

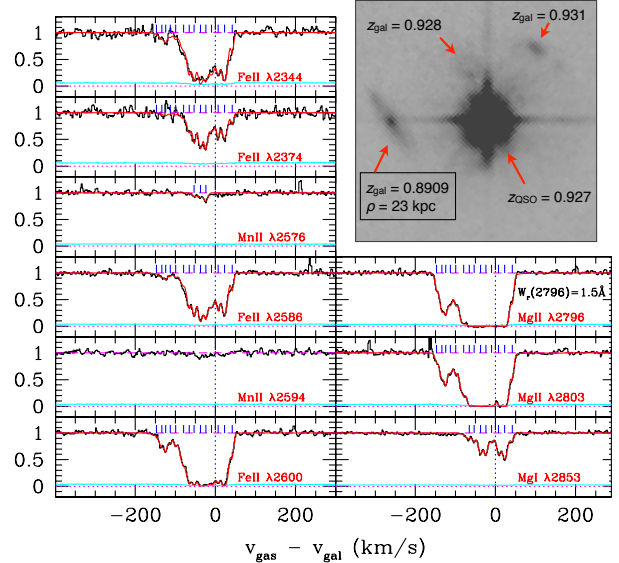


Figure 4. Line-of-sight velocity distribution of absorbing clouds at projected distance $\rho = 23 \text{ kpc}$ of Galaxy B at $z_{\text{gal}} = 0.891$ with $\alpha = 124.1$ degrees and $i_0 = 81$ degrees. We observe strong absorption in Fe II and Mg II transitions. Mn II and Mg I absorption features are also detected at the redshift of the galaxy, but are weak. Zero velocity in each spectral panel corresponds to the systemic redshift of the galaxy at $z_{\text{gal}} = 0.8909$. A Voigt profile analysis of all the observed absorption features together yields a minimum of 14 individual absorption components and $\chi_r^2 = 1.1$. The total rest-frame Mg II absorption equivalent width over all observed components is $W_r(2796) = 1.5 \text{ \AA}$. The absorbing clumps display relative line-of-sight motions ranging from $\Delta v_{\text{los}} = +42.2 \text{ km s}^{-1}$ to $\Delta v_{\text{los}} = -147.2 \text{ km s}^{-1}$ with respect to the systemic redshift of the galaxy. The absorbing galaxy is located to the left of the QSO in the image panel.

sorption complex in Fe II and Mg II transitions. Mn II and Mg I absorption features are also detected, but are weak. A Voigt profile analysis that takes into account all the observed absorption transitions yields a minimum of 14 individual absorption components and $\chi_r^2 = 1.1$. The total rest-frame Mg II absorption equivalent width over all observed components is $W_r(2796) = 1.53 \pm 0.05 \text{ \AA}$. The absorbing clumps display relative line-of-sight motions ranging from $\Delta v_{\text{los}} = +42.2 \text{ km s}^{-1}$ to $\Delta v_{\text{los}} = -147.2 \text{ km s}^{-1}$ with respect to the systemic redshift of the galaxy.

Figure 4 shows that the cool gas probed by the Mg II absorption transitions exhibits both blueshifted and redshifted motion with respect to the star-forming disk with a total line-of-sight velocity spread of $\approx 190 \text{ km s}^{-1}$. Following the discussion for Galaxy A in § 4.1, the position angle of the galaxy $\alpha = 124.1$ degrees from the QSO line of sight requires that the opening angle be greater than $\theta_0 \approx 35$ degrees in order for outflows to be responsible for the observed absorption features in the QSO spectrum. However, the presence of both blueshifted and redshifted components along the QSO sightline provides little constraint for the maximum opening angle of the outflow. We place a limit at $\theta_0 \approx 78$ degrees, beyond which because the inferred z -height blows up to unrealistic values.

Following the discussion in § 4.1, we can calculate the allowed values for the z -height and de-projected velocity of

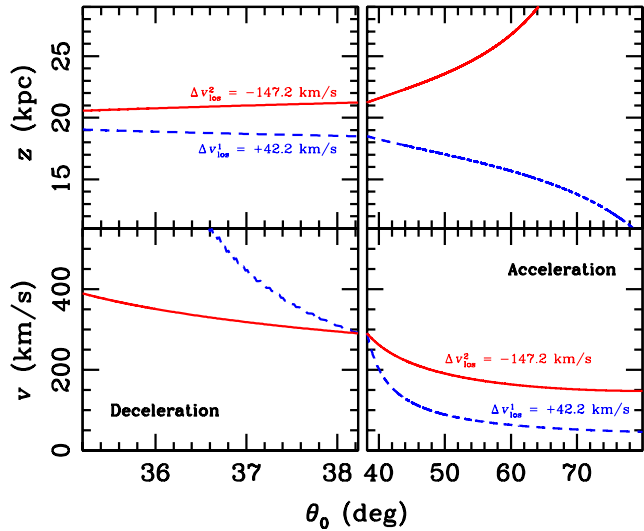


Figure 5. Allowed parameter space for the z -heights (top panels) and de-projected velocities (bottom) of individual absorbing components observed in Figure 4 versus allowed opening angle θ_0 . The minimum allowed θ_0 is constrained by the relative orientation of the star-forming disk with respect to the QSO sightline. As shown in Figure 4, the galaxy is oriented at a position angle of $\alpha = 124.1$ degrees from the QSO line of sight. In order for outflows to be responsible for the observed absorption features in the QSO spectrum, the minimum allowed opening angle is $\theta_0 \gtrsim 35$ degrees. The presence of both blueshifted and redshifted components along the QSO sightline provides little constraint for the maximum opening angle of the outflow. We place a limit at $\theta_0 \approx 78$ degrees, beyond which the QSO sightline would be completely enclosed within the outflows. Assuming an increasing line-of-sight velocity from z_1 to z_2 leads to deceleration for $\theta_0 \lesssim 38.2$ degrees and acceleration for larger θ_0 .

the outflows from Galaxy B by assuming that the line-of-sight velocity increases smoothly from z_1 to z_2 . The results are presented in Figure 5. Different from Galaxy A, our calculations show that the outflows from Galaxy B would be decelerating if $\theta_0 \lesssim 38.2$ degrees. Beyond $\theta_0 \approx 38.2$ degrees, an absorbing clump at z_1 would be moving at a lower velocity than those at z_2 in order to produce the observed line-of-sight velocity of $\Delta v_{\text{los}}^1 = +42.2 \text{ km s}^{-1}$. In this case, the outflows would be accelerating as the gas moves further away from the star-forming disk for a broad range of θ_0 . Similar to Galaxy A, it is straightforward to show that if we assume decreasing line-of-sight velocity from z_1 to z_2 , then the outflows can only be decelerating over the full range of allowed θ_0 .

4.3 Galaxy C at $z = 0.612$ in the field around LBQS 0058 + 0155

Galaxy C in the field around LBQS 0058 + 0155 ($z_{\text{QSO}} = 1.954$) was spectroscopically identified at $z_{\text{gal}} = 0.6120 \pm 0.0002$ by Chen et al. (2005). The galaxy is at projected distance $\rho = 7.9 \text{ kpc}$ from the QSO line of sight. Pettini et al. (2000) analyzed available HST WFPC2 images of the field (top-right panel of Figure 6) and estimated $i_0 \approx 65$ degrees for the disk (Table 1). We analyzed the images ourselves and estimated $\alpha = 113$ degrees. The echelle spectra of the

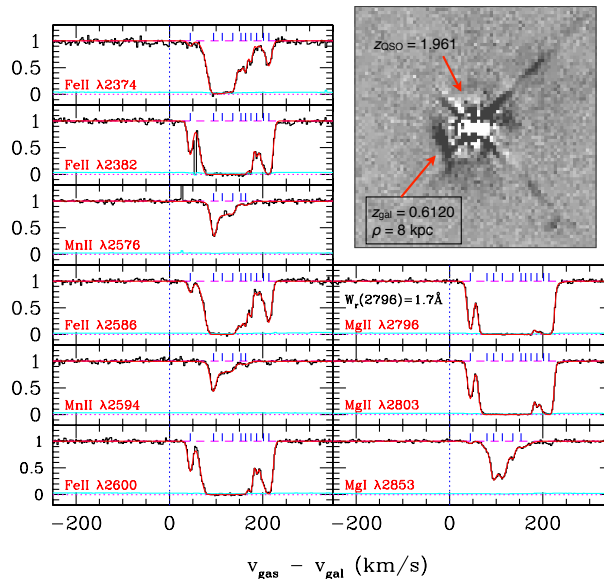


Figure 6. Line-of-sight velocity distribution of absorbing clouds at projected distance $\rho = 8 \text{ kpc}$ of Galaxy C at $z_{\text{gal}} = 0.612$ with $\alpha = 113$ degrees and $i_0 = 65$ degrees. We observe strong absorption in Fe II, Mn II, Mg II, and Mg I transitions at the redshift of the galaxy. Zero velocity in each spectral panel corresponds to the systemic redshift of the galaxy at $z_{\text{gal}} = 0.6120$. A Voigt profile analysis of the observed Fe II, Mn II, Mg II, and Mg I absorption profiles yields a minimum of 11 individual absorption components and $\chi_r^2 = 1.1$. The total rest-frame Mg II absorption equivalent width over all observed components is $W_r(2796) = 1.7 \text{ \AA}$. The absorbing clumps display relative line-of-sight motions ranging from $\Delta v_{\text{los}} = +44.9 \text{ km s}^{-1}$ to $\Delta v_{\text{los}} = +213.3 \text{ km s}^{-1}$ with respect to the systemic redshift of the galaxy. The absorbing galaxy is blended with the QSO light. The upper right panel displays the galaxy after removing the point spread function of the QSO.

QSO cover a wavelength range that allows observations of Fe II, Mn II, Mg II, and Mg I absorption at the redshift of the galaxy. The absorption profiles are shown in individual spectral panels of Figure 6. We detect a strong absorption complex in Fe II, Mn II, Mg II, and Mg I transitions. A Voigt profile analysis that takes into account all the observed absorption profiles yields a minimum of 11 individual absorption components and $\chi_r^2 = 1.1$. The total rest-frame Mg II absorption equivalent width over all observed components is $W_r(2796) = 1.67 \pm 0.01 \text{ \AA}$. The absorbing clumps display relative line-of-sight motions ranging from $\Delta v_{\text{los}} = +44.9 \text{ km s}^{-1}$ to $\Delta v_{\text{los}} = +213.3 \text{ km s}^{-1}$ with respect to the systemic redshift of the galaxy.

Figure 6 shows that the cool gas probed by the Mg II absorption transitions is entirely redshifted with respect to the star-forming disk with a total line-of-sight velocity spread of $\approx 170 \text{ km s}^{-1}$. Following the discussion in § 4.1, the position angle of the galaxy $\alpha = 113$ degrees from the QSO line of sight requires that the opening angle be greater than $\theta_0 \approx 23$ degrees in order for outflows to be responsible for the observed absorption features in the QSO spectrum. In addition, the galaxy has a inclination angle of $i_0 = 65$ degrees, and therefore the lack of blueshifted absorbing components constrains the opening angle at $\theta_0 \lesssim 35$ degrees.

Following the discussion in § 4.1, we can calculate the

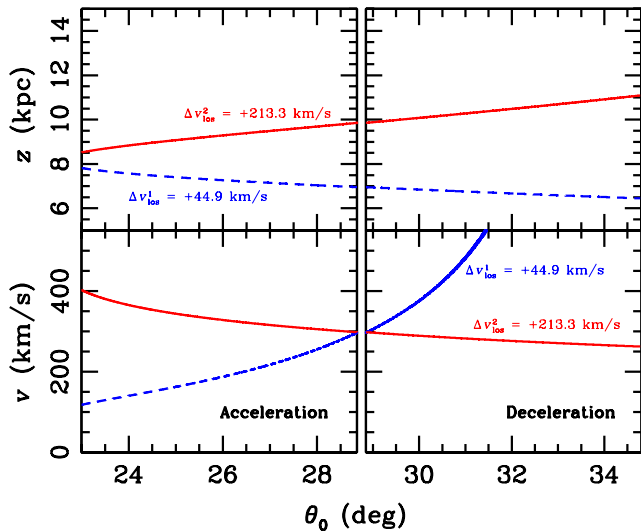


Figure 7. Allowed parameter space for the z -heights (top panels) and de-projected velocities (bottom) of individual absorbing components observed in Figure 6 versus allowed opening angle θ_0 . The minimum and maximum allowed θ_0 are constrained by the relative orientation and alignment of the star-forming disk with respect to the QSO sightline. As shown in Figure 6, the galaxy is oriented at a position angle of $\alpha = 113$ degrees from the QSO line of sight. In order for outflows to be responsible for the observed absorption features in the QSO spectrum, the minimum allowed opening angle is $\theta_0 \gtrsim 23$ degrees. In addition, all absorbing clumps are found redshifted from the systemic redshift of the galaxy. Given that the galaxy has a inclination angle of $i_0 = 65$ degrees, the lack of blueshifted absorbing components constrains the opening angle at $\theta_0 \lesssim 35$ degrees. Assuming an increasing line-of-sight velocity from z_1 to z_2 leads to acceleration for $\theta_0 \lesssim 29$ degrees and deceleration for larger θ_0 .

allowed values for the z -height and de-projected velocity of the outflows from Galaxy C by assuming that the line-of-sight velocity increases smoothly from z_1 to z_2 . The results are presented in Figure 7. Similar to Galaxy A, our calculations show that the outflows from Galaxy C would be accelerating if $\theta_0 \lesssim 29$ degrees. Beyond $\theta_0 \approx 29$ degrees, an absorbing clump at z_1 would be moving at a larger velocity than those at z_2 in order to produce the observed line-of-sight velocity of $\Delta v_{\text{los}}^1 = +44.9 \text{ km s}^{-1}$. In this case, the outflows would be decelerating as the gas moves further away from the star-forming disk. Similar to Galaxies A and B, it is straightforward to show that if we assume decreasing line-of-sight velocity from z_1 to z_2 , then the outflows can only be decelerating over the full range of allowed θ_0 .

We note that the absorber is a known damped Ly α absorption system at $z = 0.612$ with neutral hydrogen column density of $\log N(\text{HI}) = 20.1 \pm 0.2$ (Pettini et al. 2000). It is likely that a significant fraction of the observed absorption originates in the star-forming disk.

4.4 Galaxy D at $z = 0.199$ in the field toward Q0827 + 243

Galaxy D in the field around Q 0827 + 243 ($z_{\text{QSO}} = 0.939$) was spectroscopically identified at $z_{\text{gal}} = 0.199$ by Steidel et al. (2002). The nearly edge-on galaxy is at projected dis-

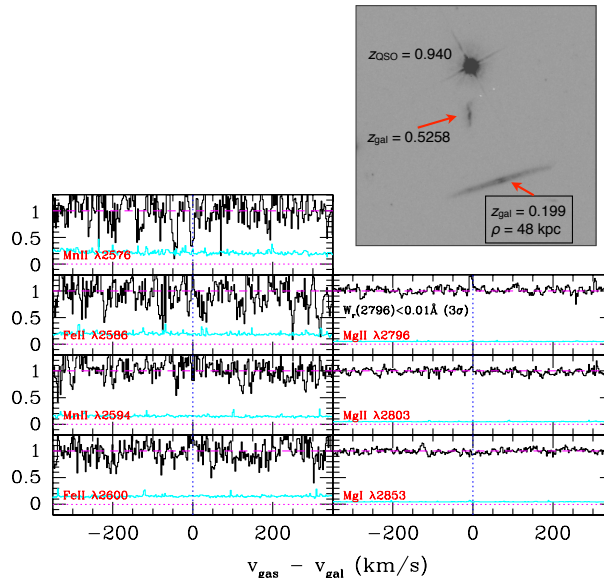


Figure 8. Absorption properties of Galaxy D at $z_{\text{gal}} = 0.199$ in the field around QSO Q0827+243. The image in the upper right panel shows a nearly edge-on galaxy at $\rho = 48$ kpc. No absorption feature is detected at the redshift of the galaxy in the QSO spectrum. We measure a $3\text{-}\sigma$ upper limit to the MgII absorption strength of $W_r(2796) = 0.01 \text{ \AA}$.

tance $\rho = 48$ kpc from the QSO line of sight. We analyzed available HST images of the field and estimated $i_0 = 85$ degrees and $\alpha = 86.3$ degrees. The echelle spectra of the QSO cover a wavelength range that allows observations of FeII, MnII, MgII, and MgI absorption at the redshift of the galaxy. However, we detect no trace of absorption features at the redshift of the galaxy in the QSO spectrum (Figure 8). We determine a $3\text{-}\sigma$ upper limit to the MgII absorption strength of $W_r(2796) = 0.01 \text{ \AA}$. The lack of absorption features associated with Galaxy D at $z_{\text{gal}} = 0.199$ implies that large-scale galactic outflows may not exist in this galaxy, despite a clear dust lane feature along the disk in the high-resolution HST image (upper right panel of Figure 8). Alternatively, the opening angle of the outflows may be small, $\theta_0 \lesssim 4$ degrees, or outflows from the star-forming disk do not reach out to ~ 50 kpc.

A second edge-on galaxy is seen at $\rho = 38$ kpc and $z_{\text{gal}} = 0.526$. This galaxy has been studied in detail by Steidel et al. (2002) and Chen et al. (2005). The major axis of this galaxy is oriented directly toward the QSO line of sight with $\alpha = 0$. We therefore exclude the galaxy from the study presented here.

5 DISCUSSION

Under the hypothesis that MgII absorbers found near the minor axis of a disk galaxy originate in the cool phase of super-galactic winds, we have carried out a study to constrain the properties of large-scale galactic outflows at redshift $z_{\text{gal}} \gtrsim 0.5$ based on the observed relative motions of individual absorbing clouds with respect to the positions and orientations of the absorbing galaxies. We have identified in the literature four highly inclined disk galaxies located

Table 2. Allowed Parameter Space for Accelerated Outflows

Galaxy	Δv_{los} (km/s)	θ_0 ($^\circ$)	z_1 (kpc)	z_2 (kpc)	v_1 (km/s)	v_2 (km/s)
A	[-54.8, -143.7]	[6.5, 9.8]	[34.7, 33.5]	[34.7, 36.1]	[200, 358]	[524, 361]
B	[+42.2, -147.2]	[38.2, 78.0]	[18.5, 10.3]	[20.2, 240.2]	[286, 46]	[289, 147]
C	[+44.9, +213.3]	[23.0, 28.9]	[7.8, 7.0]	[8.5, 9.9]	[118, 297]	[402, 297]

within 50 kpc and with the minor axis oriented within 45 degrees of a background QSO sightline. Deep HST images of the galaxies are available for accurate characterizations of the optical morphologies of the galaxies. High-quality echelle spectra of the QSO members are also available in public archives for resolving the velocity field of individual absorption clumps. All but one of the four galaxies in our study exhibit a strong associated Mg II absorption feature with $W_r(2796) \gtrsim 0.8 \text{ \AA}$ at $\rho = 8 - 34$ kpc. If super-galactic winds are present in all star-forming galaxies, then the absence of Mg II absorber to a $3\text{-}\sigma$ upper limit of $W_r(2796) = 0.01 \text{ \AA}$ at $\rho = 48$ kpc around the non-absorbing galaxy (D) indicates that either the opening angle of the outflows is small, $\theta_0 \lesssim 4$ degrees, or outflows from the star-forming disk do not reach out to ~ 50 kpc.

Combining known morphological parameters of the galaxies such as the inclination (i_0) and orientation (α) angles of the star-forming disks, and resolved absorption profiles of the associated absorbers at < 35 kpc away, we have explored the allowed parameter space for the opening angle θ_0 and the velocity field of large-scale galactic outflows as a function of z -height, $v(z)$, from each disk galaxy. In this section, we discuss the implications of our analysis.

5.1 Kinematics of Super-galactic Winds

The results of our analysis presented in § 4 show that the observed absorption signatures of the Mg II doublets and the Fe II series are compatible with the absorbing gas being either accelerated or decelerated (Figures 3, 5, & 7) for different ranges of the opening angle of the outflows. We summarize the allowed parameter space for accelerated outflows in Table 2, which lists for each galaxy the observed range of relative line-of-sight velocities of individual absorbing components with respect to the systemic velocity of the galaxy (Δv_{los}), the range of opening angle (θ_0) over which the observed velocity spread can be explained by accelerated outflows, the corresponding range of z -height above the star-forming disk (z_1) where the QSO sightline enters the accelerated outflows (Figure 1), the corresponding range of z_2 where the QSO sightline exits the outflows, and the corresponding ranges of outflowing velocities at z_1 (v_1) and z_2 (v_2).

As described in § 4, our calculations are based on the assumption that the outflow velocities follow a smooth gradient with the distance from the star-forming disk, which allows us to project the observed velocity components to the appropriate z -heights in the conical outflow model. Assuming that the observed line-of-sight velocity increases with the z -height, Table 2 shows that acceleration is valid only for a limited range of θ_0 for galaxies A and C. Beyond the

maximum allowed angle in each of the galaxies, the outflowing gas at z_1 would have to move faster than those at larger z -heights in order to reproduce the small projected velocity found along the QSO sightline. The outflows would be decelerating, instead of accelerating. For galaxy B, the upper bound for θ_0 remains unconstrained, but the inferred z -height blows up to unphysically large values at $\theta_0 = 78$ degrees.

We present in Figure 9 the observed velocity field versus z -height above the star-forming disk of each galaxy for a set of θ_0 that cover the full range of allowed θ_0 as summarized in Table 2. It is clear that for a significant fraction of allowed θ_0 , the inferred velocity gradient is extreme. A few percent gain in z -height would result in increasing outflow velocity by more than 100%, further narrowing down the range of reasonable θ_0 that would yield a more physical acceleration field.

For comparison, we consider model predictions by Murray et al. (2011; hereafter M11), who presented an analytical model for launching large-scale galactic winds. These authors showed that radiation pressure from the most massive star clusters in the disk can clear holes in the disk, allowing subsequent supernovae ejecta to escape the disk. As the outflowing material is lifted above the disk, the combined influence of radiation and ram pressure forces from multiple star clusters would then accelerate the winds further out to several tens of kpc away from the disk.

M11 provided model predictions for different types of galaxies, including M82, the Milky Way and luminous starburst galaxies at $z \sim 2$. For each galaxy type, the authors considered the effect of different physical parameters on the kinematics of outflowing gas, including the ram pressure drag force due to the hot supernova winds and the mass of super star clusters. Given that the galaxies in our sample are sub- L_* galaxies (Table 1), we will focus our comparisons on the M82-like models.

Specifically, we adopt the predicted velocity field from M11 for large-scale galactic outflows that are driven by the combined influence of radiation and ram pressure forces of a super star cluster of $10^6 M_\odot$ in an M82-like galaxy. The dot-dashed curves in Figure 9 indicate the predictions for different feedback efficiencies $\epsilon\beta$, where ϵ is the fraction of the supernova luminosity that is thermalized to produce a hot phase and β is the mass loading factor limited within the range, $1 \leq \beta \leq 17$. In the absence of a ram pressure drag force, the predicted velocity field is represented by the solid curve in Figure 9 with $\epsilon\beta = 0$.

Figure 9 shows that in order for the M11 model to be consistent with observations, the allowed θ_0 are further reduced to a narrow range, where the inferred acceleration is minimal. Namely, $\theta_0 \approx 10$ degrees for galaxy A, $\theta_0 \approx 38$

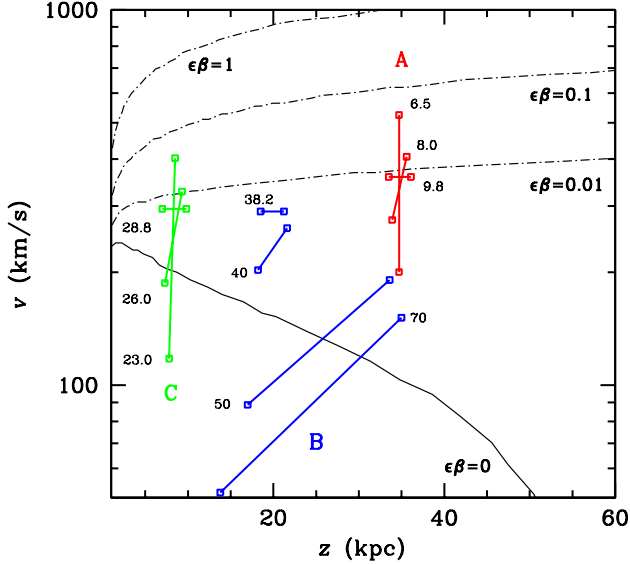


Figure 9. Comparisons between the deprojected outflow velocities as a function of z -height $v(z)$ observed around star-forming disks and model predictions for accelerated outflows. For each galaxy, we present the velocity range and the corresponding z -height in the large-scale outflows for a set of θ_0 that cover the full range of allowed θ_0 as summarized in Table 2. Each set of data points is labeled by the corresponding θ_0 . It is clear that for a significant fraction of allowed θ_0 the inferred velocity gradient is extreme, increasing outflow velocity by more than 100% for only a few percent gain in z -height. We adopt model predictions from Murray et al. (2011), who calculated the velocity field of super-galactic winds driven by the radiation and ram pressure forces from a stellar cluster of $10^6 M_\odot$ in an M82-like galaxy. The dot-dashed curves are for different feedback efficiencies $\epsilon\beta$, where ϵ is the fraction of the supernova luminosity that is thermalized to produce a hot phase and β is the mass loading factor limited within the range, $1 \leq \beta \leq 17$. In the absence of a ram pressure drag force, the predicted velocity field is shown in the solid curve with $\epsilon\beta = 0$. We find that for every galaxy the Murray et al. model can explain the observations for only a narrow range of θ_0 where the inferred acceleration is minimal. Namely, $\theta_0 \approx 10$ degrees for galaxy A, $\theta_0 \approx 38$ degrees for galaxy B, and $\theta_0 \approx 29$ degrees for galaxy C. At these specified opening angles, the feedback efficiency is small with $\epsilon\beta \lesssim 0.01$.

degrees for galaxy B, and $\theta_0 \approx 29$ degrees for galaxy C. At these specified θ_0 , the observations also favor a small feedback efficiency with $\epsilon\beta \lesssim 0.01$.

The narrow range of favored θ_0 from the model comparisons in Figure 9 is understood by the expected decline of radiation and ram pressure forces at distances beyond 1 kpc (Figure 2 in M11). To characterize the declining acceleration as a function of z -height, we consider a power-law model following the parameterization of Steidel et al. (2010) (see also Veilleux et al. (1994) who adopted a similar parametrization),

$$a(z) = A z^{-\alpha}. \quad (6)$$

If we designate z_{\min} as the launch z -height of super-galactic winds, then we can recast Equation (6) in terms of the outflows velocity field as

$$v(z) = \left(\frac{2A}{\alpha - 1} \right)^{1/2} \sqrt{z_{\min}^{1-\alpha} - z^{1-\alpha}}. \quad (7)$$

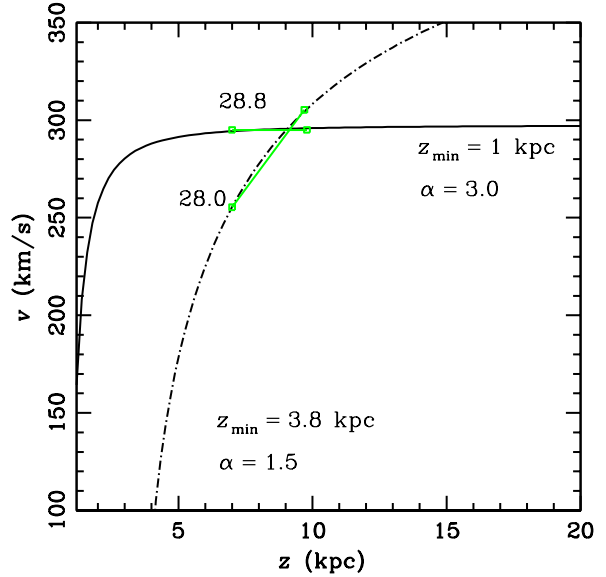


Figure 10. Examples to illustrate the appropriate power-law model for characterizing accelerated outflows inferred for our sample galaxies. We consider two specific cases for galaxy C at $\rho = 7.9$ kpc. As summarized in Table 2, the allowed opening angle of accelerated outflows in this galaxy is $\theta_0 = 23 - 28.9$ degrees. The plot shows the derived $v(z)$ for $\theta_0 = 28.8$ degrees and $\theta_0 = 28$ degrees. In order to reproduce the constant velocity field at $z \approx 10$ kpc for an opening angle of $\theta_0 = 28.8$ degrees, the acceleration model formulated in Equations (6) and (7) should have a steep power-law index of $\alpha = 3$ for a launch radius of $z_{\min} = 1$ kpc. To reproduce the large velocity gradient implied by a slightly smaller opening angle $\theta_0 = 28$ degrees requires a launch radius of $z_{\min} = 3.8$ kpc for a shallower power-law index $\alpha = 1.5$ that is more typical of what is found in $z_{\text{gal}} = 2 - 3$ starburst galaxies (Steidel et al. 2010). For smaller θ_0 , the velocity gradient steepens (Figure 9). While the shallower power-law index is a viable solution, the launch radius would approach $z_{\min} \approx 7.5$ kpc. By analogy, we conclude that adopting a shallower power-law index $\alpha \lesssim 2$ for characterizing the accelerated outflows in galaxies A & B (Figure 9) would require a launch radius $z_{\min} \gtrsim 20$ kpc.

Steidel et al. (2010) found that the acceleration model defined in Equations (6) and (7) with $\alpha = 1.15 - 1.95$ and $z_{\min} = 1$ kpc can reproduce the blueshifted self-absorption of low-ionization transitions found in luminous starburst galaxies at $z_{\text{gal}} = 2 - 3$.

To explore the power-law index α and launch radius z_{\min} appropriate for describing the accelerated outflows in our sample in Figure 9, we consider two specific cases for galaxy C at $\rho = 7.9$ kpc. As summarized in Table 2, the allowed opening angle of accelerated outflows in this galaxy is $\theta_0 = 23 - 28.9$ degrees. Figure 10 displays the derived $v(z)$ for $\theta_0 = 28.8$ and $\theta_0 = 28$ degrees. At $\theta_0 = 28.8$ degrees, the conical outflows model expects that the QSO sightline probes outflowing gas from $z_1 = 7.9$ kpc to $z_2 = 11.2$ kpc with little change in the outflow velocity. At $\theta_0 = 28$ degrees, the conical outflows model expects that the QSO sightline probes outflowing gas from $z_1 = 7.9$ kpc to $z_2 = 11$ kpc with the outflow velocity increasing from $v_1 = 255 \text{ km s}^{-1}$ to $v_2 = 305 \text{ km s}^{-1}$.

Following the acceleration model formulated in Equations (6) and (7),

Table 3. Allowed Parameter Space for Decelerated Outflows

Galaxy	Δv_{los} (km/s)	θ_0 ($^\circ$)	z_1 (kpc)	z_2 (kpc)	v_1 (km/s)	v_2 (km/s)
A	[-54.8, -143.7] [-143.7, -54.8]	[9.8, 17.3] [6.5, 17.3]	[33.5, 32.1] [34.7, 32.1]	[36.1, 37.9] [34.7, 37.9]	[361, 5085] [525, 13335]	[361, 270] [200, 103]
B	[+42.2, -147.2] [-147.2, +42.2]	[35.2, 38.2] [35.2, 78.0]	[19.0, 18.5] [19.0, 10.3]	[20.6, 21.2] [20.6, 240.2]	[4320, 291] [15070, 160]	[390, 290] [112, 42]
C	[+44.9, +213.3] [+213.3, +44.9]	[28.9, 34.8] [23.0, 34.8]	[7.0, 6.4] [7.8, 6.4]	[9.9, 11.1] [8.5, 11.1]	[297, 7708] [559, 36617]	[298, 262] [85, 55]

tions (6) and (7), to reproduce the constant velocity field at $z \approx 10$ kpc for an opening angle of $\theta_0 = 28.8$ degrees requires a steep power-law index of $\alpha = 3$ for a launch radius of $z_{\text{min}} = 1$ kpc. To reproduce the large velocity gradient implied by a slightly smaller opening angle $\theta_0 = 28$ degrees requires a launch radius of $z_{\text{min}} = 3.8$ kpc for a shallower power-law index $\alpha = 1.5$ that is more typical of what is found in $z_{\text{gal}} = 2 - 3$ starburst galaxies (Steidel et al. 2010). As summarized in Table 2, the allowed opening angle of galaxy C for accelerated outflows can be as small as $\theta_0 = 23$ degrees. For $\theta_0 = 23$ degrees, the shallower power-law index is a viable solution but the launch radius needs to increase to $z_{\text{min}} \approx 7.5$ kpc. By analogy, we conclude that adopting a shallower power-law index $\alpha \lesssim 2$ for characterizing the accelerated outflows in galaxies A & B would require a launch radius $z_{\text{min}} \gtrsim 20$ kpc.

In summary, we have shown that acceleration is only possible for a limited range of θ_0 , if we project the velocity components to the appropriate z -height assuming that the observed line-of-sight velocity increases with z -height. Under an acceleration scenario, the observations favor a narrow range of model parameters such as $\epsilon\beta \lesssim 0.01$, and $\alpha \approx 3$ for $z_{\text{min}} = 1$ kpc or $\alpha \approx 1.5$ for $z_{\text{min}} \gtrsim 4$ kpc. For θ_0 outside of the range summarized in Table 2, we have shown that the gas would be decelerating, because a larger speed is required at smaller z -height in order to reproduce the small projected velocity along the QSO sightline. In addition, if we adopt an inverse mapping between the line-of-sight velocity and z -height, namely if the observed line-of-sight velocity decreases with increasing z -height, then the outflows would only be decelerating over the full range of allowed θ_0 . It is clear that the allowed parameter space for decelerated outflows is significantly broader than what is shown in Table 2, but Figures 3, 5, & 7 have shown that beyond certain θ_0 the de-projected velocity in the outflows exceeds 1000 km s^{-1} at $z > 10$ kpc which also seem unphysical. A summary for decelerated outflows is presented in Table 3.

5.2 Implications for the Origin of Super-Galactic Winds

We have shown that combining known inclination (i_0) and orientation (α) angles of the star-forming disks and resolved absorption profiles of the associated absorbers at projected distances $\rho = 8 - 35$ kpc, we can derive strong constraints for the opening angle θ_0 , the velocity field of large-scale galactic outflows $v(z)$ which leads to constraints for the supernova feedback efficiency $\epsilon\beta \lesssim 0.01$, and the acceleration param-

eters α and z_{min} . Here we examine whether these parameter constraints are reasonable and discuss their implications.

First, we consider the allowed opening angle θ_0 for accelerated outflows. Table 2 shows that with the exception of galaxy B, for which the upper bound of θ_0 remains unconstrained, both galaxies A and C are constrained to have $\theta_0 < 10$ and $\theta_0 < 30$ degrees, respectively, for the outflows probed by Mg II and Fe II absorption transitions. These allowed values of θ_0 are smaller than the typical opening angle of $2\theta_0 \approx 60 - 135$ degrees seen in nearby starburst galaxies (e.g. Veilleux et al. 2005). The discrepancy can be understood, if there exist a tilt or asymmetries around the minor axis in the outflows (e.g. Shopbell & Bland-Hawthorn 1998; Sugai et al. 2003), in which case the opening angle of the outflows in our galaxies may be bigger. In addition, we note that these constraints are derived for Mg II absorbing gas which presumably traces the cool phase of super-galactic winds. Hot galactic winds can be more wide spread than the cool clumps. Numerical simulations have shown that cool clouds embedded in a supersonic wind are broken up to form elongated filamentary structures (Cooper et al. 2009). The small θ_0 found in our study may be understood, if the Mg II absorbers are produced in these elongated filaments.

Next, we consider the constraint for supernova feedback efficiency $\epsilon\beta \lesssim 0.01$. Recall that in the Murray et al. (2011) model, ϵ is the fraction of the supernova luminosity that is thermalized to produce a hot phase and β is the mass loading factor which by definition must be $\beta > 1$. The constraint we found therefore requires that the efficiency of thermal energy input from supernova explosion to be $\epsilon < 0.01$. This is significantly smaller than both the thermalization efficiency estimated for M82 ($0.3 \leq \epsilon \leq 1$) by Strickland & Heckman (2009) and those found in numerical simulations (e.g. $\epsilon \approx 0.2$ from Thornton et al. 1998). We note, however, that the model is only compatible with the observations for a special value of θ_0 in each case. A significant fraction of the allowed θ_0 would yield a steeper velocity gradient, increasing velocity at larger z -height, that is incompatible with the expectations of the model. Such discrepancy suggests that if the gas is being accelerated, then additional forces are necessary.

Finally, we consider the constraints for the power-law acceleration field. We have shown that the inferred $v(z)$ for different allowed θ_0 under an acceleration scenario requires that either the superwinds are launched close to the star-forming disk with $z_{\text{min}} = 1$ kpc but a steeply declining acceleration $a(z) \propto z^{-3}$ or they are launched at large distances with $z_{\text{min}} \gtrsim 4$ kpc and $a(z) \propto z^{-1.5}$. The latter applies

for most allowed θ_0 . Other mechanisms for launching supergalactic winds include cosmic ray pressure (e.g. Pfrommer et al. 2007; Everett et al. 2008), but whether or not cosmic rays can explain a launch z -height beyond 4 kpc is unclear.

In summary, we have considered in detail the scenario of accelerated outflows for explaining the observed gas kinematics of strong Mg II absorbers. We have derived the first empirical constraints for super-galactic winds at $z_{\text{gal}} \gtrsim 0.5$ that can be compared directly with model predictions. Our analysis has uncovered an interesting parameter space that is largely incompatible with current models for driving accelerated outflows on galactic scales. Decelerated outflows can explain the observed velocity field, but the inferred velocity gradients (see Table 3) are significantly steeper than expected from momentum-driven wind models (e.g. Dijkstra & Kramer 2012).

A competing scenario is that some or all of the absorbing gas originates in infalling halo gas or a larger co-rotating disk. Unfortunately given the large degree of freedom in the spatial distribution and trajectory of infalling clouds, we cannot place meaningful constraints on the infall velocity field. On the other hand, Lanzetta & Bowen (1992) have demonstrated that absorption-line systems tracing co-rotating disks are expected to exhibit an “edge-leading” profile with the peak absorbing component occurring at the largest velocity offset and declining absorbing strength toward the systemic velocity of the absorbing galaxy. Given that none of the galaxy-absorber pairs in our sample shows such edge-leading profiles, we can rule out the scenario of the absorbing gas following an organized rotation motion around the central galaxy.

Lastly, given available observations of QSO absorption line systems at low redshifts (the COS-Halos survey – e.g., Tumlinson et al. 2011), we expect that a similar analysis like the one presented in this paper can be conducted for a larger sample of galaxies for which HST images are available. In particular, the UV spectra obtained by the Cosmic Origins Spectrograph cover both high- and low-ionization transitions (e.g., Si II, CIV, and OVI) which offer additional constraints for the kinematics of the hot circumgalactic medium over a range of stellar masses and star formation histories.

ACKNOWLEDGMENTS

We thank C. Steidel, R. Trainor, and Y. Matsuda for helpful discussions during the early stages of this project. We thank O. Agertz, N. Gnedin, A. Kravtsov, M. Rauch, G. Rudie, W. Sargent, and A. Wolfe for helpful comments on an earlier version of the paper. We also thank C. Steidel for providing the optical spectrum of galaxy B in our study. JRG gratefully acknowledges the financial support of a Millikan Fellowship provided by Caltech and of a Grant-In-Aid of Research from the National Academy of Sciences, administered by Sigma Xi, The Scientific Research Society.

REFERENCES

Adelberger, K. L., Shapley, A. E., Steidel, C. C., Pettini, M., Erb, D. K., & Reddy, N. A. 2005, *ApJ*, 629, 636

- Aguirre, A., Hernquist, L., Schaye, J., Weinberg, D. H., Katz, N., & Gardner, J. 2001, *ApJ*, 560, 599
- Bland-Hawthorn, J., Veilleux, S., & Cecil, G. 2007, *Ap&SS*, 311, 87
- Bond, N. A., Churchill, C. W., Charlton, J. C., & Vogt, S. S. 2001, *ApJ*, 562, 641
- Bordoloi, R., et al. 2011, *ApJ*, 743, 10
- Cen, R., Nagamine, K., & Ostriker, J. P. 2005, *ApJ*, 635, 86
- Chelouche, D., & Bowen, D. V. 2010, *ApJ*, 722, 1821
- Chen, H.-W., Helsby, J. E., Gauthier, J.-R., Shectman, S. A., Thompson, I. B., & Tinker, J. L. 2010a, *ApJ*, 714, 1521
- Chen, H.-W., Wild, V., Tinker, J. L., Gauthier, J.-R., Helsby, J. E., Shectman, S. A., & Thompson, I. B. 2010b, *ApJ*, 724, L176
- Chen, H.-W., Kennicutt, R. C. Jr., & Rauch, M. 2005, *ApJ*, 620, 703
- Chen, H.-W., Lanzetta, K. M., Webb, J. K., & Barcons, X. 2001b, *ApJ*, 559, 654
- Chen, H.-W., Lanzetta, K. M., & Webb, J. K. 2001a, *ApJ*, 556, 158
- Chen, H.-W., Lanzetta, K. M., Webb, J. K., & Barcons, X. 1998, *ApJ*, 498, 77
- Cooper, J. L., Bicknell, G. V., Sutherland, R. S., & Bland-Hawthorn, J. 2008, *ApJ*, 674, 157
- Cooper, J. L., Bicknell, G. V., Sutherland, R. S., & Bland-Hawthorn, J. 2009, *ApJ*, 703, 330
- Davé, R., Oppenheimer, B. D., Katz, N., Kollmeier, J. A., & Weinberg, D. H. 2010, *MNRAS*, 408, 2051
- Dekel, A., & Silk, J. 1986, *ApJ*, 303, 39
- Dijkstra, M., & Kramer, R. 2012, arXiv:1203:3803
- D’Odorico, S., Cristiani, S., Dekker, H., Hill, V., Kaufer, A., Kim, T., & Primas, F. 2000, in *Society of Photo-Optical Instrumentation Engineers (SPIE) Conference Series*, Vol. 4005, *Society of Photo-Optical Instrumentation Engineers (SPIE) Conference Series*, ed. J. Bergeron, 121–130
- Everett, J. E., Zweibel, E. G., Benjamin, R. A., McCammon, D., Rocks, L., & Gallagher, III, J. S. 2008, *ApJ*, 674, 258
- Gauthier, J.-R., & Chen, H.-W. 2011, *MNRAS*, 418, 2730
- Heckman, T. M., Lehnert, M. D., Strickland, D. K., & Armus, L. 2000, *ApJS*, 129, 493
- Heckman, T. M. 2002, in *Astronomical Society of the Pacific Conference Series*, Vol. 254, *Extragalactic Gas at Low Redshift*, ed. J. S. Mulchaey & J. T. Stocke, 292
- Jones, T., Stark, D. P., & Ellis, R. S. 2011, *ArXiv e-prints*
- Kacprzak, G. G., & Churchill, C. W. 2011, *ApJ*, 743, L34
- Lanzetta, K. M., & Bowen, D. V. 1992, *ApJ*, 391, 48
- Martin, C. L., & Bouché, N. 2009, *ApJ*, 703, 1394
- Matejek, M. S., & Simcoe, R. A. 2012, *ArXiv e-prints*
- Murray, N., Ménard, B., & Thompson, T. A. 2011, *ApJ*, 735, 66
- Murray, N., Quataert, E., & Thompson, T. A. 2005, *ApJ*, 618, 569
- Nestor, D. B., Johnson, B. D., Wild, V., Ménard, B., Turnshek, D. A., Rao, S., & Pettini, M. 2011, *MNRAS*, 412, 1559
- Oppenheimer, B. D., & Davé, R. 2006, *MNRAS*, 373, 1265
- Oppenheimer, B. D., Davé, R., & Finlator, K. 2009, *MNRAS*, 396, 729

- Pettini, M., Ellison, S. L., Steidel, C. C., Shapley, A. E., & Bowen, D. V. 2000, *ApJ*, 532, 65
- Pfrommer, C., Springel, V., Jubelgas, M., & Ensslin, T. A. 2007, in *Astronomical Society of the Pacific Conference Series*, Vol. 379, *Cosmic Frontiers*, ed. N. Metcalfe & T. Shanks, 221
- Pieri, M. M., Martel, H., & Grenon, C. 2007, *ApJ*, 658, 36
- Rubin, K. H. R., Prochaska, J. X., Ménard, B., Murray, N., Kasen, D., Koo, D. C., & Phillips, A. C. 2011, *ApJ*, 728, 55
- Rubin, K. H. R., Weiner, B. J., Koo, D. C., Martin, C. L., Prochaska, J. X., Coil, A. L., & Newman, J. A. 2010, *ApJ*, 719, 1503
- Rupke, D. S., & Veilleux, S. 2005, *ApJ*, 631, L37
- . 2005a, *ApJS*, 160, 87
- Shopbell, P. L., & Bland-Hawthorn, J. 1998, *ApJ*, 493, 129
- Steidel, C. C., Dickinson, M., Meyer, D. M., Adelberger, K. L., & Sembach, K. R. 1997, *ApJ*, 480, 568
- Steidel, C. C., Erb, D. K., Shapley, A. E., Pettini, M., Reddy, N., Bogosavljević, M., Rudie, G. C., & Rakic, O. 2010, *ApJ*, 717, 289
- Steidel, C. C., Kollmeier, J. A., Shapley, A. E., Churchill, C. W., Dickinson, M., & Pettini, M. 2002, *ApJ*, 570, 526
- Strickland, D. K., & Heckman, T. M. 2009, *ApJ*, 697, 2030
- Sugai, H., Davies, R. I., Ward, M. J. 2003, *ApJ*, 584, L9
- Thornton, K., Gaudlitz, M., Janka, H.-T., & Steinmetz, M. 1998, *ApJ*, 500, 95
- Tremonti, C. A., Moustakas, J., & Diamond-Stanic, A. M. 2007, *ApJ*, 663, L77
- Tumlinson, J., Thom, C., Werk, J. K., Prochaska, J. X., Tripp, T. M., Weinberg, D. H., Peebles, M. S., O'Meara, J. M., Oppenheimer, B. D., Meiring, J. D., Katz, N. S., Davé, R., Ford, A. B., & Sembach, K. R., 2011, *Science*, 334, 948
- Veilleux, S., Cecil, G., Bland-Hawthorn, J., Tully, R. B., Fillipenko, A. V., & Sargent, W. L. W., 2004, *ApJ*, 433, 48
- Veilleux, S., Cecil, G., & Bland-Hawthorn, J. 2005, *ARA&A*, 43, 769
- Weiner, B. J., et al. 2009, *ApJ*, 692, 187
- Zibetti, S., Ménard, B., Nestor, D. B., Quider, A. M., Rao, S. M., & Turnshek, D. A. 2007, *ApJ*, 658, 161